Transport in Porous Media
https://doi.org/10.1007/s11242-020-01399-9

Wall Effect Mitigation Techniques for Experiments with Planar Walls

Eric J. Roth[1] · **Roseanna M. Neupauer**[1] · **David C. Mays**[2] · **Lauren J. Sather**[1] · **John P. Crimaldi**[1]

Received: 22 July 2019 / Accepted: 25 February 2020

Abstract
Experiments in porous media suffer from preferential flow along apparatus walls—called the *wall effect*—which results from higher porosity and therefore higher permeability near the walls. Through a theoretical analysis of porosity in a three-dimensional rectangular apparatus containing spherical beads with hexagonal close packing, this study shows that porosity, and therefore wall effects, exhibits different behavior along each of the orthogonal walls. This study also experimentally evaluates two techniques for mitigating wall effects in experiments of solute transport in porous media using monodisperse, spherical beads in hexagonal close packing as the bulk porous medium. The first mitigation technique adds a sublayer of smaller beads of one third of the diameter of the primary beads between the wall and the bulk media. The second mitigation technique applies a half-bead-diameter-thick layer of silicone to the wall and embeds one layer of beads into the silicone, creating a wall of hemispheres. Both techniques seek to impose more uniform porosity up to the wall. Velocity profiles indicate that both techniques eliminate preferential flow along the wall and therefore are effective at mitigating the wall effect.

Keywords Wall effect · Hexagonal close packing · Refractive-index matching · Laser-induced fluorescence · Preferential flow

1 Introduction

Experiments of flow and transport in porous media are often conducted by packing porous media into a bench-scale container. Examples include permeameters to estimate permeability by measuring head loss across a column, column experiments to estimate dispersivity from measured breakthrough curves (Robbins 1989), and quasi-two-dimensional experiments to observe flow and transport, often using refractive-index matched

✉ John P. Crimaldi
crimaldi@colorado.edu

[1] Department of Civil, Environmental, and Architectural Engineering, University of Colorado Boulder, UCB 428, Boulder, CO 80309-0428, USA

[2] Department of Civil Engineering, University of Colorado Denver, Campus Box 113, PO Box 173364, Denver, CO 80217-3364, USA

Published online: 28 February 2020

porous media and fluid combinations (Stohr et al. 2003; Werth et al. 2010; Wright et al. 2017). Unfortunately, the apparatus used in the experiments described above all suffer from the so-called *wall effect*, i.e., preferential flow adjacent to smooth walls resulting from non-uniform packing of the porous material near the apparatus walls, which can contribute to significant experimental error (Cohen and Metzner 1981).

Media packing becomes less dense in proximity to the wall due to the transition from an unbounded media structure in the interior to a truncated structure with increased void volume along the planar surface of the wall. For example, for round granular media, porosity at the interface between the media and a smooth apparatus wall approaches unity (Cohen and Metzner 1981; Schwartz and Smith 1953; Eisfeld and Schnitzlein 2001; Gunn 1987).

As the local porosity increases, the local permeability within the porous media also increases. In approximately monodisperse, spherical media, permeability, k, can be estimated using the Kozeny–Carman equation (Carman 1937) given by

$$k = \frac{n^3}{(1-n)^2} \frac{\left(d_{50}\right)^2}{180} \tag{1}$$

where n is porosity, and d_{50} is the median grain diameter. Equation (1) indicates that permeability is primarily controlled by porosity for monodisperse granular media. Thus, along an apparatus wall, where local porosity is higher than the bulk porosity, local permeability will be higher than the bulk permeability. Since velocity is proportional to permeability, higher permeability near the apparatus walls leads to higher velocities near the walls. For example, Schwartz and Smith (1953) found that near-wall velocities are 30–100% higher than the velocity in the bulk porous media.

To limit the impact of the wall effect on the experimental results, some experimental protocols only analyze regions that are sufficiently far from apparatus walls, approximately 6 grain diameters away from the wall for one-dimensional flow (Cohen and Metzner 1981; de Klerk 2003). Others apply a correction factor during the data analysis phase (Cohen and Metzner 1981; Eisfeld and Schnitzlein 2001). Alternatively, the wall effect can be directly mitigated by implementing a strategy to match the near-wall porosity to the average porosity of the bulk porous media, which would lead to near-wall velocities that essentially match the velocity in the bulk porous media. One such mitigation technique has been proposed by Mcwhirter et al. (1997), in which grains were embedded in the wall. Unfortunately, the efficacy of the proposed technique was not confirmed experimentally. Although techniques for mitigating wall effects have been suggested, we are unaware of any published experimental testing of these techniques.

In this work, we perform a laboratory investigation of the effects of two techniques for mitigating wall effects in a rectangular, smooth-walled glass chamber filled with spherical beads with hexagonal close packing (HCP). The two mitigation techniques include filling extra near-wall pore space with either smaller beads or silicone. We evaluate wall effect mitigation by comparing near-wall fluid velocity to the bulk velocity. To do this, we fill the pore space with a refractive-index matched fluid, and track the movement of a dye tracer in the fluid. We use laser-induced fluorescence to image the dye movement through the chamber both with and without wall mitigation techniques.

Theoretical analysis of local porosity for hexagonal close packing near apparatus walls is provided in Sect. 2. The experimental apparatus, wall mitigation techniques, and the data analysis are described in Sect. 3. Velocity profiles from experiments with and without mitigation techniques, which demonstrate the efficacy of those mitigation techniques, are

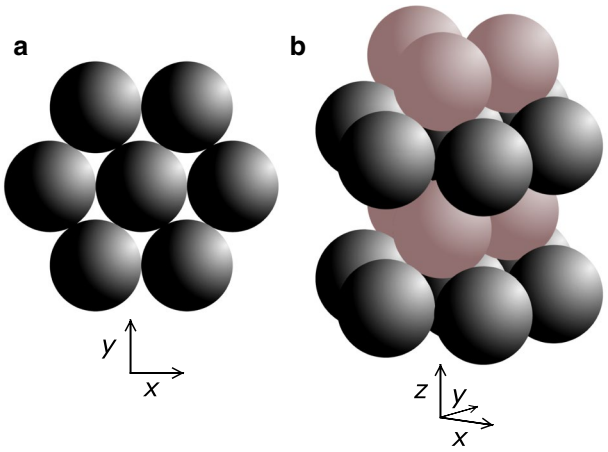

Fig. 1 Hexagonal close packing (HCP) of spheres. **a** Plan view of a single layer. **b** Oblique view of a unit cell comprising four layers of spheres, with each layer of like-colored spheres having the same positioning in the x–y plane. Spheres are offset by one half of a sphere diameter in the x direction and by $1/\sqrt{3}$ of a sphere diameter in the y direction relative to spheres in the overlying and underlying layers

reported in Sect. 4. Sections 5 and 6 provide discussion and conclusions, and the porosity relationships reported in Sect. 2 are derived in the "Appendix".

2 Theoretical Analysis of Porosity with Hexagonal Close Packing

HCP, a close packing geometry that can be easily implemented for monodisperse spheres, produces nearly homogeneous packing within bulk porous media. In experiments, this quality makes it possible to accurately distinguish between flow behavior in the bulk porous media from that near the wall. HCP packing of monodisperse spheres has a theoretical porosity of 0.26 (Smith et al. 1929); however, in practice the packing structure, and therefore the porosity, deviates from HCP at the apparatus walls. For example, McWhirter et al. (1998) and Smith et al. (1929) report that porosity typically ranges from 0.35 to 0.45 in experiments due in part to rigid walls that upset packing geometry. The specific packing structure near a wall depends on the orientation of the wall relative to the main HCP layer structure. Consider the packing in Fig. 2, which shows a horizontal projection of two layers of spheres packed with hexagonal close packing, adjacent to the corner of a rectangular prismatic container. With layers numbered in the $+z$ direction, the light-colored spheres

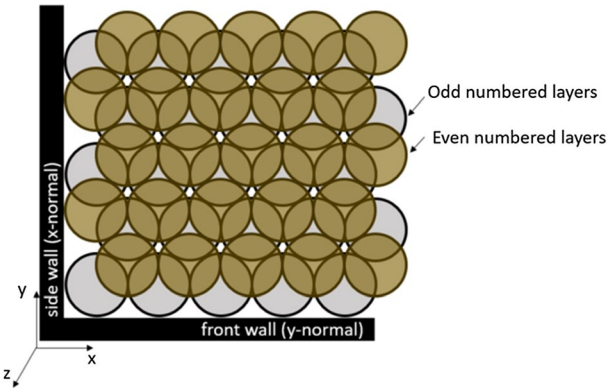

Fig. 2 Horizontal projection of two layers of spheres with HCP packing in the vicinity of the front and side walls. Light circles (gray in online version) represent odd-numbered layers, numbered sequentially from the bottom. Darker circles (tan in online version) represent the even-numbered layers. See "Appendix" for details

(gray in online version) represent Layer 1, which is the bottom layer and assumed to be resting on a flat plane at $z=0$, following the configuration shown in Fig. 1a. The dark-colored spheres (tan in online version) represent the second layer of spheres in the z direction, which are resting in the valleys created by three gray spheres, as shown in Fig. 1b. The alternating layers of light-colored and dark-colored spheres continue in the z direction (see Fig. 1b).

Figure 2 shows that the packing along the walls deviates from the packing in the interior of the container, with extra void space near the wall where a grain would otherwise be in the absence of a solid boundary. For this particular packing structure, Fig. 3 shows plots of areal porosity as a function of distance from the x-normal, y-normal, and z-normal walls, relative to the bead diameter d (see "Appendix" for details). We use the terminology x-normal wall, y-normal wall, and z-normal wall to define the walls parallel to the y–z (normal to the x-direction), x–z plane, and x–y planes, respectively.

Porosity is unity at the wall and decreases away from the wall. Beyond a certain distance from the wall (shown in Fig. 3), porosity exhibits a repetitive pattern, where the average porosity is equal to the theoretical porosity of 0.26 for HCP. Note that the near-wall porosities are different for each wall, therefore each wall experiences different wall effects. For HCP using the defined coordinate system, the z-normal wall exhibits the lowest porosity as compared to the other walls. This is due to the fact that HCP does not have right angles (Fig. 1), while the apparatus does. While each layer in the x–y plane is identical, each layer is shifted diagonally from neighboring layers. Therefore, packing against the z-normal wall presents differently than packing against the x- or y-normal walls (see "Appendix" for further details on HCP geometry for each wall).

3 Experimental Methods

3.1 Apparatus

The experimental apparatus shown in Fig. 4 includes a one-dimensional flow chamber that contains porous media, fluid, and dye; a laser to induce fluorescence of the dye; and

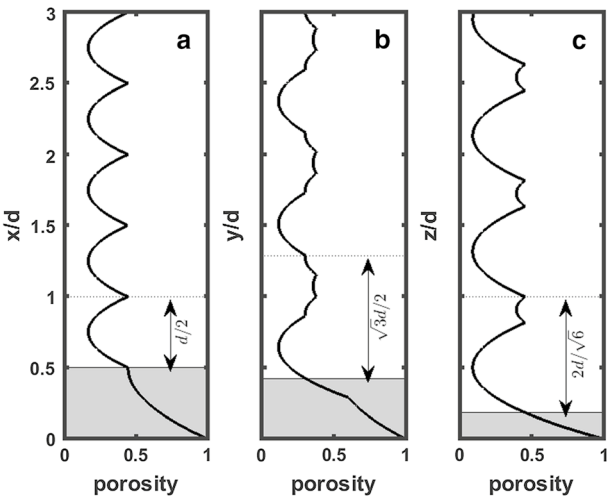

Fig. 3 Porosity as a function of distance from **a** the x-normal wall, **b** the y-normal wall, and **c** the z-normal wall. The shaded gray box represents the region where porosity is impacted by proximity to the wall. The labeled arrows represent the interval of repetition. The bead diameter is denoted as d

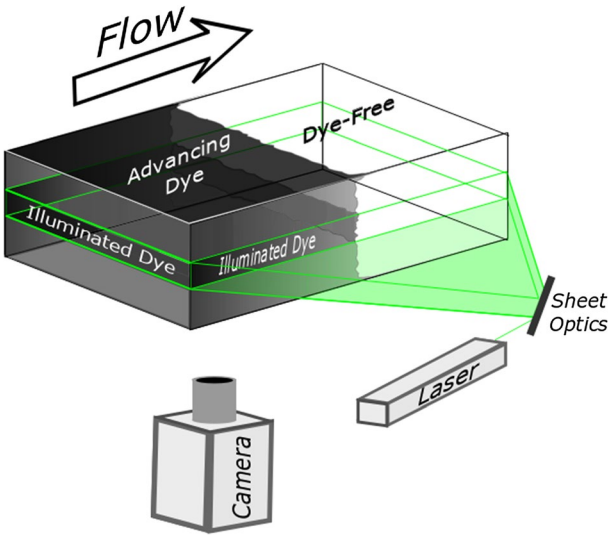

Fig. 4 Schematic of one-dimensional flow apparatus

a camera to capture images of the dye movement. The porous media are 3 mm diameter, borosilicate glass beads (Pyrex, part# 7268-3), that were systematically placed into the flow chamber to obtain HCP packing. Glycerin (99.7% USP Glycerin, Chemworld, CAS# 56-81-5) was chosen as the fluid. Glycerin and borosilicate glass both have a refractive index of 1.47 at room temperature, making the fluid-bead system essentially transparent and allowing optical access through the flow chamber. A fluorescent dye solution of Rhodamine 6G (Aldrich, CAS# 989-38-8) dissolved in glycerin was used as a tracer. The addition of dye did not have a measurable impact on the refractive index of the glycerin.

The glycerin and beads were contained in a quasi-one-dimensional flow test section constructed from a glass box measuring 17 cm × 8 cm × 7 cm (Fig. 4). On either side of the test section, flow entrance and exit chambers were bounded by an aluminum screen with a large mesh size to minimize perturbed flow, while simultaneously holding the beads firmly in place. The bead packing within the test section was nearly homogeneous HCP. Deviations from theoretical HCP were due to variations in bead size, typically ± 3% of the nominal bead diameter, and not due to bead misalignment. Porosity was measured at the conclusion of each experiment (see Roth 2018 for the protocol). The measured porosity range was 0.314–0.347, which is below the typical range of 0.35–0.45 found in other experiments (Smith et al. 1929; McWhirter et al. 1998) and closer to the theoretical porosity of 0.26 for HCP. Although it is practically impossible to achieve the minimum theoretical porosity, because of slightly non-uniform bead diameters and the disruption to the HCP pattern imposed by the fixed walls, nevertheless the low porosity measured at 0.314–0.347 indicates a high degree of homogeneity for a matrix containing monodisperse spheres.

A 514 nm laser was passed through a beam expander (Melles Griot, 25x-10x) and single-axis scanning-galvo-mirror (Thorlabs, GVS011) to create a 1-cm-thick laser sheet that illuminated the dye within the test section containing the porous media (Fig. 4), causing it to fluoresce. A camera (Imperx, ICL-B1410M-SCO), oriented perpendicular to the laser sheet, captured images of dye fluorescence. An optical band-pass filter (Omega Optics, 555DF30) was attached to the camera lens, blocking the 514 nm excitation light from the laser while transmitting fluoresced light from the dye. The resulting image showed

fluorescent emission intensity from the dye present within the laser sheet only. The imaged intensity is proportional to the dye concentration (Crimaldi 2008).

Prior to the start of the experiment, the solution of dye and glycerin was preloaded into the entrance chamber and segregated from the beads in the test section by a plastic curtain. Simultaneously, the beads were saturated with dye-free glycerin. Immediately prior to data collection, the plastic curtain was pulled back to allow dye to flow into the test section, supplied by a continuous flow of identical dye–glycerin solution injected into the entrance chamber upstream of the porous media at a flow rate of approximately 5 mL/min, from a gear pump (Ismatek, model# CB 78008, with Cole-Parmer model# 73004-14 pump head). Dye–glycerin solution entered the porous media as a continuous planar source. Fluid passed through the exit chamber, then left the apparatus through an outlet left open to the atmosphere 2 cm above the top elevation of the bulk porous media. Throughout the experiment, the entire apparatus, including the entrance and exit chambers, was kept saturated at a head equivalent to 2 cm of glycerin controlled by the outlet condition.

For these experiments, pore-scale Reynolds number was calculated for the bulk porous media within the chamber by

$$R = \frac{d\rho}{\mu} v. \tag{2}$$

The density, ρ, and dynamic viscosity, μ, of glycerin at 20 °C are 1.26 g/cm^3 and 14.9 g/cm-s, respectively. Velocity, $v = 4.5 \times 10^{-3}$ cm/s, was calculated by using the average measured porosity of 0.33, the flow rate of 5 ml/min (used in all experiments), and by assuming uniform flow through the 8 cm × 7 cm cross section. Reynolds number for these experiments is approximately 1.2×10^{-4}. Diffusivity, D, for Rhodamine 6G in glycerin at 20 °C was calculated using the Stokes–Einstein equation:

$$D = \frac{k_B T}{6\pi\mu r}. \tag{3}$$

where k_B is Boltzmann's constant, and T is the absolute temperature. The radius of a spherical particle, r, corresponds with a molecule of Rhodamine 6G dye. Assuming that the Rhodamine 6G particle has a radius of 7.7×10^{-8} cm (as calculated from the diffusivity of Rhodamine 6G in water), calculated diffusivity for Rhodamine 6G dye in glycerin was 1.9×10^{-9} cm^2/s. Peclet number, P, was calculated by

$$P = \frac{d}{D} v. \tag{4}$$

Peclet number for these experiments is approximately 7.2×10^5.

3.2 Wall Effect Mitigation

Two techniques were tested to mitigate wall effects by modifying the near-wall porosity to reduce the local permeability and preferential flow along apparatus walls. In the first technique, near-wall porosity was approximately matched to that in the bulk porous media by placing 1-mm borosilicate glass beads (Chemglass, part# CG-1101-06), with diameters equal to 1/3 times that of the bulk media, into the interstitial volume between the wall and the first layer of 3-mm beads, as shown in Fig. 5b. The refractive index of the 1-mm beads matched that of the bulk porous media and the fluid, so optical access

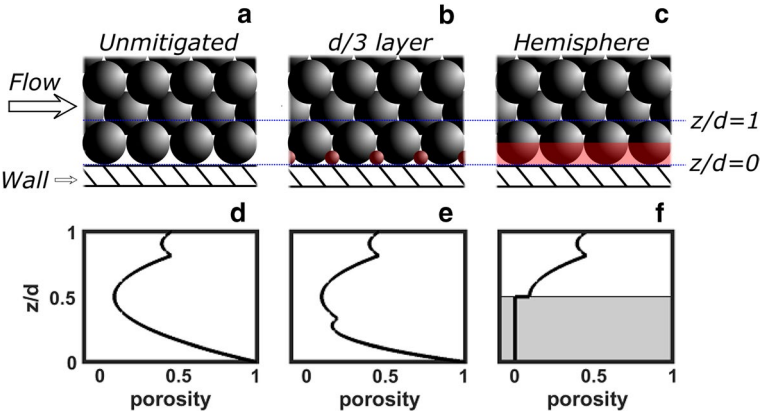

Fig. 5 Schematic of vertical cross section above z-normal wall for **a** unmitigated wall, **b** $d/3$ bead layer, and **c** hemisphere wall. Porosity as a function of distance from the z-normal wall for **d** unmitigated wall, **e** $d/3$ bead layer, and **f** hemisphere wall, note that the pore space within the shaded region is filled with silicone and is therefore not within the flow domain

through this wall was preserved. Since this mitigation technique adds a layer of beads whose diameter is 1/3 of the diameter of the main beads, we call this mitigation technique the "$d/3$ bead layer".

To install the $d/3$ bead layer, a guide was built by gluing a single HCP layer of 3-mm beads to an aluminum plate with dimensions matching those of the z-normal face of the apparatus test section. A second layer of 3-mm beads was placed in the guide in an HCP geometry controlled by the preceding rigid layer and held in place by gravity. Individual 1-mm beads were then placed into the interstitial volumes of the second 3 mm layer. The apparatus was then turned upside down, and the loaded bead guide was lifted upward into the inside of the apparatus, such that the 1 mm sublayer was in contact with the z-normal face of the test section. With the guide held firmly in place, the chamber and guide were righted together, such that the 1-mm beads were at the lowest elevation, followed by a 3 mm HCP layer, and the guide. The guide was removed, allowing the 1-mm and 3-mm beads to maintain HCP configuration (see "Appendix" for details).

Subsequent bead layers were then loaded in the HCP configuration by gently shaking the apparatus at different orientations. The HCP geometry was confirmed for each bead in the layer before adding beads for subsequent layers. It should be noted that packing geometry for each of the two y-normal walls will be different. During HCP loading, one of the y-normal walls will preferentially be used for bead alignment while adding additional HCP layers, resulting in a "tightly packed" y-normal configuration. Due to inherent mismatches between HCP geometry and the rigid boundary imposed by the geometry of the test section, the opposite y-normal wall will exhibit a "loosely packed" configuration.

The second wall effect mitigation technique is similar to that suggested by Mcwhirter et al. (1997). First, the volume of the test chamber was completely packed with HCP beads. A uniform layer of wet silicone (GE, 100% Silicone II, Black) was then applied to the lid of the apparatus by using a screed and spacers to ensure a consistent depth. The silicone on the lid was then pressed into the pre-packed beads, resulting in an opaque wall of hemispheres which preserved HCP packing (Fig. 5c). We call this mitigation technique the "hemisphere wall". With this configuration, both porosity and permeability are uniform

throughout the entire domain, at the expense of losing optical access through the opaque silicone.

Figure 5d–f shows the theoretical distribution of areal porosity as a function of distance from the z-normal wall for the unmitigated wall and for the two wall mitigation techniques. Both wall mitigation techniques theoretically result in a lower near-wall porosity. For the hemisphere technique, considering the volume above the silicone, the porosity exactly matches the pattern present within the bulk porous media (Fig. 3). While the $d/3$ technique does not exactly match the porosity pattern within the bulk porous media, the average porosity for $z/d < 0.5$ nearly matches the measured average porosity of the bulk porous media in our experiments.

3.3 Image Analysis

Throughout the experiments, two-dimensional images of the depth-integrated intensity of fluoresced dye, which is proportional to dye concentration, were collected within the x–y plane at a frequency of 1 frame every 10 s. Thus, the images show the propagation of the dye front through the apparatus. Although the flow rate through the chamber was controlled by a pump and therefore was known, the dye velocity varies in the direction transverse to flow as a result of wall effects. However, flow can be assumed to be one-dimensional everywhere (for justification, see Sect. 4).

Under assumptions of one-dimensional flow in a homogeneous porous material in a semi-infinite domain, with constant dye concentration of C_o entering at $x = 0$, the dye concentration, $C(x, t)$ is given by (Ogata and Banks 1961)

$$\frac{C(x,t)}{C_o} = \frac{1}{2}\left[\operatorname{erfc}\left(\frac{x - vt}{2\sqrt{Dt}}\right) + \exp\left\{\frac{vx}{D}\right\}\operatorname{erfc}\left(\frac{x + vt}{2\sqrt{Dt}}\right)\right] \tag{5}$$

where v is average linear velocity in the region unaffected by wall effects and D is the dispersion coefficient. Neglecting terms in (2) that account for boundary effects, $C/C_o = 0.5$ at $x = vt$; thus the velocity as a function of position in the direction transverse to flow can be obtained by dividing the domain into narrow slices parallel to flow and tracking the position where $C/C_o = 0.5$ (defined here as x_{50}) for each slice. Slice width was equal to $d/2$ for $z/d \leq 2$ and equal to d for $z/d > 2$. Linear regression performed on a plot of x_{50} versus time was used to estimate the velocity for each slice (an example of this method can be seen in Fig. 6). The influence of the wall effects was also evaluated qualitatively by visually identifying the region where the dye front was not perpendicular to the flow direction.

4 Results

4.1 Wall Effect

First we present results to demonstrate that each unmitigated wall produces a different wall effect because of different local porosity variations. Figures 7 and 8 show images of normalized dye concentration at three different times during two different experiments with no wall effect mitigation. Figure 7 shows the results for z-normal wall packing geometry as defined in Fig. 2; while Fig. 8 shows the results for the y-normal wall packing geometry (tightly packed). In both experiments, the beads were packed the same way, with $z = 0$ as

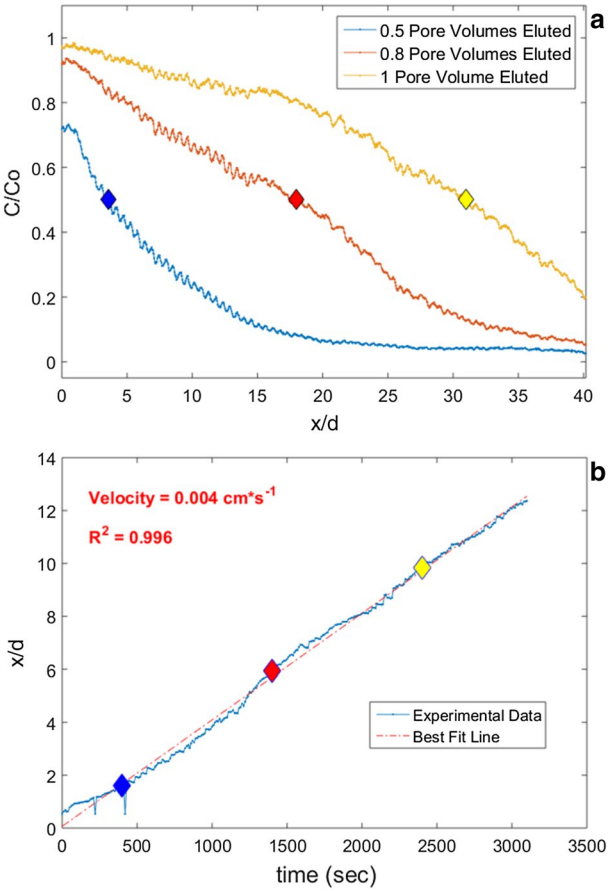

Fig. 6 Example of method to estimate average linear velocity. **a** C/C_o for the experiment with the unmitigated z-normal wall at three times after introduction of dye for $5 < z/d < 6$. Note that the region near the planar dye source was cropped for analysis due to non-uniform bead loading near the entrance chamber. The diamonds identify the points on the curve where $C = C_o/2$, and $x = x_{50}$ at each time. **b** x_{50} versus time and best-fit line. The slope of the best-fit line is the velocity for $5 < z/d < 6$. The diamonds correspond to the points taken from subplot a

the base of the apparatus; however, in the experiment shown in Fig. 7, the apparatus was rotated 90° about the x-axis so that the wall effect along the z-normal walls could be analyzed. Preferential flow near the wall is evident in the depth-integrated (over the axis parallel to the viewing angle) images of C/C_o from both unmitigated wall experiments. Velocities in the bulk porous media, beyond approximately 0.5 bead diameters from the wall, are also relatively uniform for both cases. However, within 0.5 bead diameters to the wall, velocity is much higher. For example, in Figs. 7b and 8b, the dye near the wall ($z/d = 0$ and $y/d = 0$, respectively) reaches the downstream boundary ($x/d = 40$) after only 0.5 pore volumes of dye were eluted, while the dye front in the bulk porous media has only traveled to $x/d \approx 10$.

Figures 7 and 8 also provide evidence that the bead packing was homogeneous. For regions sufficiently far from the apparatus walls, i.e., approximately 2 bead diameters, the advection front remained approximately planar and perpendicular to the direction of flow. If the packing were heterogeneous, one would expect to see a non-perpendicular advection front, indicating a systematic change in packing with depth, or the formation of preferential pathways into the bulk porous media. Image analysis shows that velocities in the bulk porous media are relatively uniform for regions beyond one bead diameter from the wall for the y-normal wall, and beyond 0.5 bead diameters for

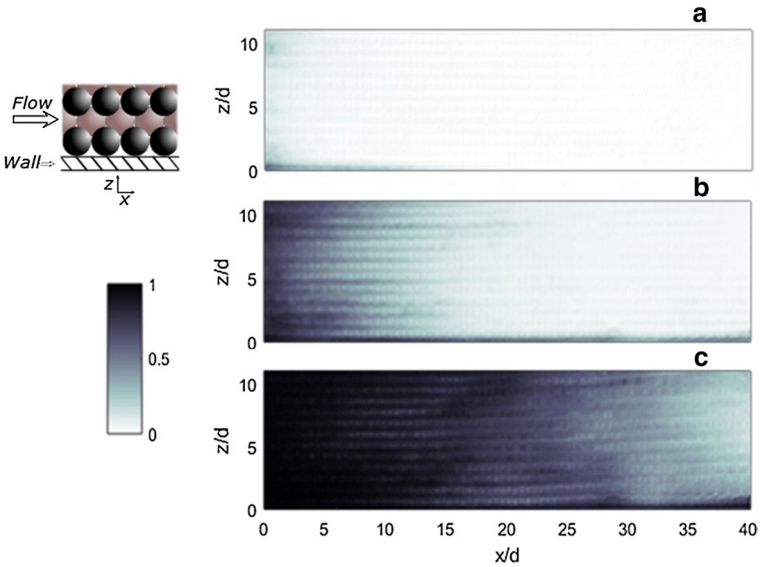

Fig. 7 C/C_o images for unmitigated wall effect along the z-normal wall as shown in Fig. 5a after **a** 0.2 pore volumes eluted, **b** 0.5 pore volumes eluted, **c** 1 pore volume eluted. The wall is located at $z/d=0$

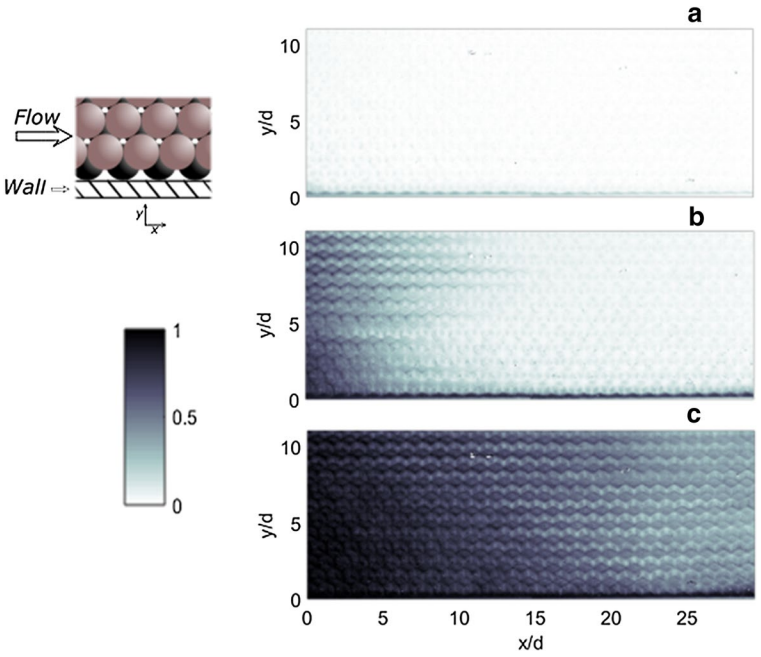

Fig. 8 C/C_o images for unmitigated wall effect along the y-normal wall as shown in Fig. 5a after **a** 0.2 pore volumes eluted, **b** 0.5 pore volumes eluted, **c** 1 pore volume eluted. The wall is located at $y/d=0$

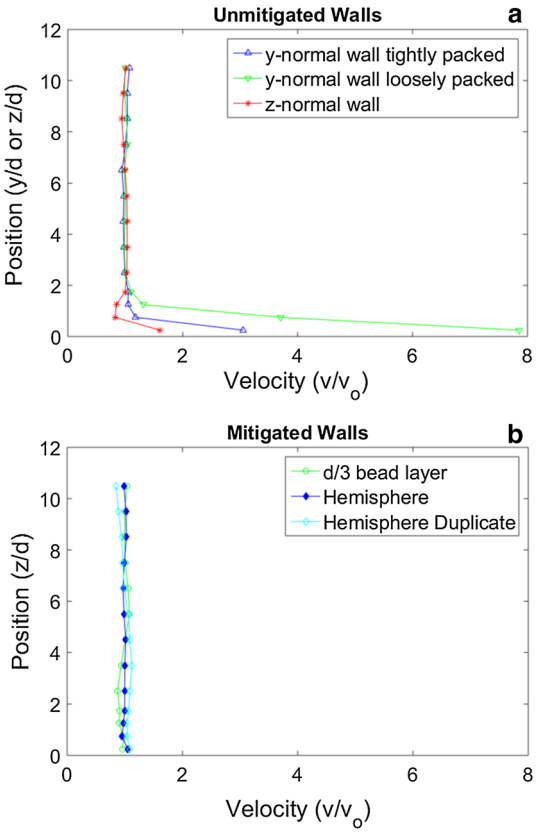

Fig. 9 Normalized velocity profiles as a function of distance from the **a** y-normal and z-normal unmitigated walls. **b** z-normal wall with mitigation. v_o is the velocity in the bulk porous media

the z-normal wall (Fig. 9a). The z-normal wall exhibits a near-wall velocity that is 60% higher than the average velocity in the bulk porous media. The y-normal walls exhibit near-wall velocities 200% and 700% higher than the average velocity in the bulk porous media for tightly and loosely packed walls, respectively. These results are consistent with the theoretical porosity distributions in Fig. 3b, c. The presence of the wall affects porosity over a larger distance in the y-normal direction than in the z-normal direction. Since higher porosity produces higher permeability, which in turn leads to higher velocity, the theory predicts that the lowest velocity would occur along the z-normal wall, and the highest velocity would occur along the y-normal wall with loose packing.

It should be noted that the experiment uses physical media which will inherently have some slight variation in bead diameter, as well as slight imperfections in packing. From a practical perspective, the bead packing in the physical apparatus would be less uniform than what was assumed in the theoretical model. Also, the data shown for the y-normal wall with loosely packed media in Fig. 9 exhibit a farther-reaching wall effect relative to the y-normal wall with tightly packed media. The loosely packed wall represents a condition where rigid apparatus walls do not perfectly match the dimensions of the porous media bed, leading to looser packing near the wall.

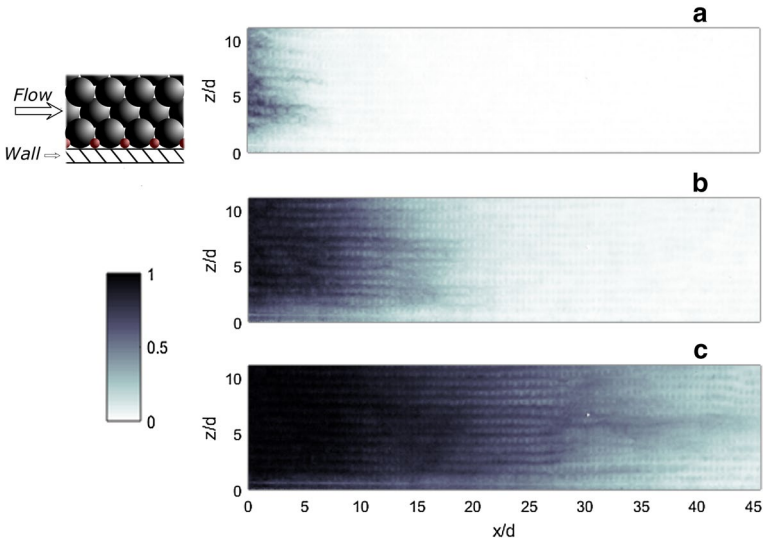

Fig. 10 C/C_o images for mitigated wall effect using the $d/3$ wall treatment along the z-normal wall as shown in Fig. 5a after **a** 0.2 pore volumes eluted, **b** 0.5 pore volumes eluted, **c** 1 pore volume eluted. The wall is located at $z/d=0$

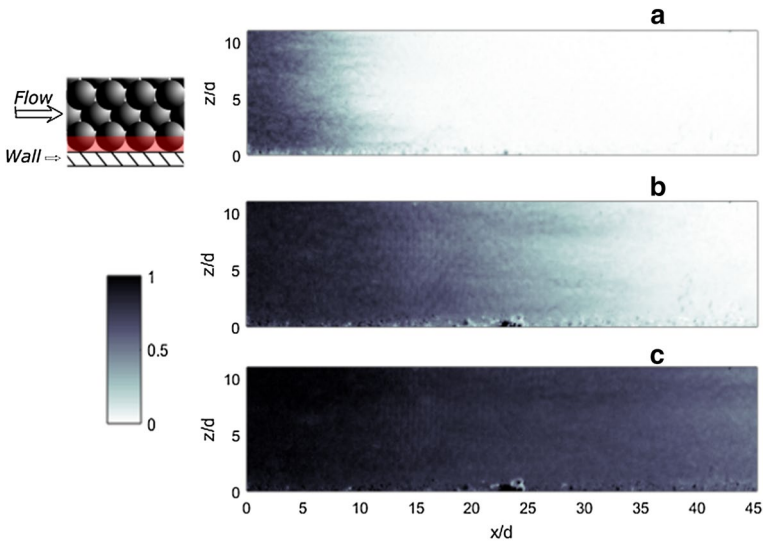

Fig. 11 C/C_o images for mitigated wall effect using the hemisphere wall treatment along the z-normal wall as shown in Fig. 5a after **a** 0.2 pore volumes eluted, **b** 0.5 pore volumes eluted, **c** 1 pore volume eluted. The wall is located at $z/d=0$

4.2 Wall Effect Mitigation

Figures 10 and 11 show images of normalized dye concentration at three different times during experiments with the two mitigation techniques. In both cases, the dye along the wall travels at the same rate as the dye in the bulk porous media, in contrast to the fast-moving dye along the walls in the experiments with unmitigated walls (compare Figs. 10b and 11b with Figs. 7b and 8b). These results demonstrate that both mitigation techniques eliminated the preferential flow near the wall. For the *d*/3 layer mitigation technique, the near-wall velocity appears lower than the velocity in the bulk porous media (Fig. 10); however this behavior was caused by a non-planar dye source distribution in this particular experiment. Note that data were only gathered within a center 1 cm × 7 cm thick slice of the apparatus for the *x*-normal walls, or center 1 cm × 8 cm thick slice for the *y*-normal walls within the 17 cm × 8 cm × 7 cm apparatus. These slices were illuminated by the laser sheet, capturing fluid dynamics for only two of the walls parallel to flow for each experiment, and approximately 15% of the total cross-sectional area parallel to flow. Therefore, flow velocities along two of the walls parallel to flow were unknown. Flow rate through the bulk porous media can change dramatically due to variations in packing density (contributing to variations in preferential flow) along the unmeasured walls for each experiment. So even though all experiments were performed with the same inlet flow rate, velocity through the measurement area can vary across experiments. In addition, porous media packing near the upstream and downstream walls of the apparatus (normal to flow) was non-uniform due to the screen material used at the boundary. Therefore, data near the entrance and exit of the bulk porous media was not included in the analysis.

Figure 9b shows the velocity profiles based on image analysis of both wall effect mitigation techniques. In both cases, the near-wall velocities are approximately equal to average velocities in the bulk porous media. These results provide additional evidence that both wall mitigation techniques eliminate preferential flow near the walls, and therefore eliminate the wall effects. Note that preferential flow paths are present in the bulk porous media due to the structure of the HCP. These flow paths are caused by oscillating porosity patterns (Fig. 3). All of the data shown in Fig. 9 are averaged over a width larger than *d*/4, a resolution that does not show the effects of this uniform, oscillatory behavior.

5 Discussion

The wall effect mitigation techniques discussed in this paper were developed and used for quasi-two-dimensional solute transport experiments. These techniques also should prove valuable for other applications that use granular media within a system with flat walls—at least on the floor and the ceiling (i.e., *z*-normal walls) of the apparatus, defined from the perspective of loading the granular media. Within the context of groundwater hydrology, the accuracy of granular media experiments could be improved using these methods. For industrial applications, these techniques could be employed to improve the efficiency of fixed bed reactors.

To our knowledge, the *d*/3 diameter sphere mitigation technique used to preserve RIM optical access in porous media has not been proposed by other researchers. While the embedded bead technique was proposed by Mcwhirter et al. (1997), we did not find experimental implementation of the technique in the literature. Based on reported porosity in the literature,

we could find no evidence of an HCP loading as precise as ours. The qualitative results of the physical experiments are consistent with theory. In addition, we found no experimental evidence in the literature to support expectations from theory.

These wall effect mitigation treatments could potentially be extended to other applications, particularly within apparatus that do not use flat boundaries. For this situation, it may be possible to insert the $d/3$ spheres concurrently with the primary diameter spheres that constitute the bulk porous media using application-specific equipment. The hemisphere wall treatment could be applied to any apparatus surface prior to media packing using specific media packing protocols such as silicone application devices specifically designed to accommodate the geometry of the apparatus.

6 Conclusions

The HCP loading used in the experiments produced homogeneous porous media, evident from minimal porosity measurements and from uniform flow velocities for regions sufficiently far from apparatus walls. Dependent upon precision of media loading and bead uniformity, for one-dimensional flows within HCP porous media, flow will not be significantly affected by wall effects for regions beyond one bead diameter from side walls and beyond 0.5 bead diameters from base walls. While this result is in agreement with the theoretical analysis presented in this text, it is somewhat inconsistent with the conventional wisdom that wall effects extend 4–6 bead diameters from smooth walls (Cohen and Metzner 1981, de Klerk 2003). This discrepancy is likely due to the highly uniform packing used in experiments, leading to enhanced media heterogeneity near the wall (as shown theoretically in Fig. 3). If packing is less uniform near the wall, which is likely for most porous media experiments, the wall effect likely would extend farther into the bulk porous media. Similarly, in our experiments velocities near the walls were 60–700% higher than average velocities in the bulk porous media, significantly higher than the 30–100% increase found in other studies. This is most likely due to the use of more densely packed media in our experiments, creating a sharper contrast between porosity within the bulk media and the near-wall regions, with the wall effect occupying a smaller portion of the total cross-sectional area normal to flow. Due to conservation of mass, the reduction in cross-sectional area encompassed by the wall effect will lead to higher velocities along the walls relative to experiments with less densely packed porous media.

This study investigated two wall effect mitigation strategies, both of which were successful at producing near-wall velocities that were approximately equal to average velocities in the bulk porous media. In conclusion, these techniques should allow researchers to overcome the wall effect, that is, to eliminate preferential flows near walls. For homogeneously packed test sections, these techniques should accurately model unbounded porous media systems subject to one- or two-dimensional flow.

Acknowledgements The authors gratefully acknowledge the two anonymous reviewers whose comments improved the paper. Funding was provided by the National Science Foundation under Grants EAR-1417005 and EAR-1417107.

Appendix: Areal Porosity Near Walls

Figure 12 shows a horizontal projection of two layers of spheres packed with hexagonal close packing in a three-dimensional, rectangular prismatic box, with the light-colored spheres (gray in online version) on the bottom (Layer 1) and the dark-colored spheres (tan in online version) in the layer above (Layer 2). The white triangles in Fig. 12 are used in Fig. 13 to determine the offsets between spheres in the same layer and between two spheres in adjacent layers, which are used below to calculate areal porosity. Let the coordinates of the center of Spheres G (in Layer 1) and T (in Layer 2) be (x_G, y_G, z_G) and (x_T, y_T, z_T), respectively. By inspection, $x_T - x_G = d/2$. From Fig. 13, $y_T - y_G = d/\left(2\sqrt{3}\right)$. Setting the

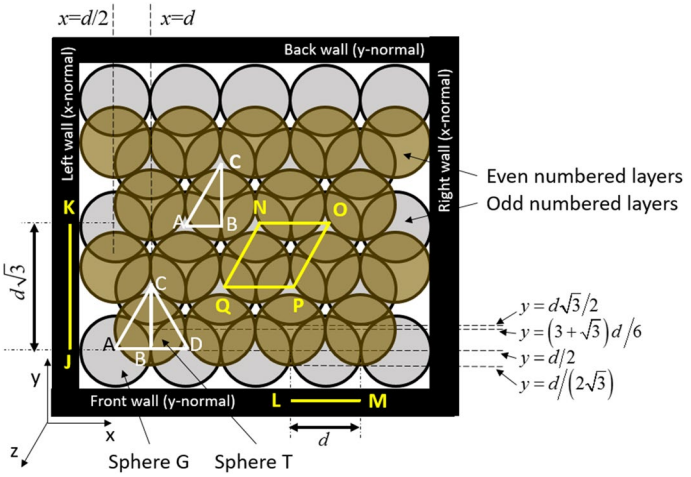

Fig. 12 Horizontal projection of two layers of spheres with HCP packing in a rectangular box. Light circles (gray in online version) represent odd-numbered layers of spheres, numbered sequentially from the bottom. Dark circles (tan in online version) represent the even-numbered layers of spheres. The angles and side lengths of triangles ABC and ACD are presented in Fig. 13. Line JK is a projection of a control surface in the *y*–*z* plane; Line LM is a projection of a control surface in the *x*–*z* plane; and Trapezoid NOPQ is a control surface in the *x*–*y* plane

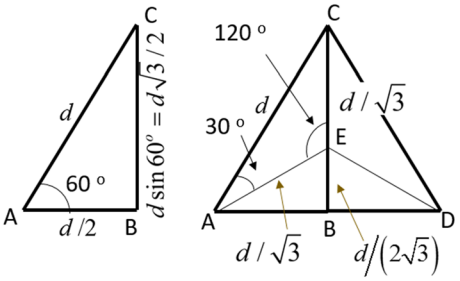

Fig. 13 Trigonometry of triangles ABC and ACD in Fig. 12. Vertices A, C, and D represent centers of spheres in the odd-numbered layers (light circles in Fig. 12), and Vertex B represents a point of contact between two such spheres. Point E is equidistant from vertices A, C, and D, and is situated directly below the center of a sphere in the even-numbered layers (dark circles in Fig. 12). The lengths of AE, CE, and DE are found from the law of sines as $\overline{AE} = \sin 30^\circ\, d/\sin 120^\circ = d/\sqrt{3}$

distance between the centers of Spheres G and T to d leads to $z_T - z_G = 2d/\sqrt{6}$. Although not shown in the figure, the alternating of gray and tan layers continues in the z direction (as shown in Fig. 1b), with the bottom elevation of Layer j equal to $z = 2(j-1)d/\sqrt{6}$.

The areal porosity, $n(s)$, in a plane parallel to the s-normal wall is given by

$$n(s) = \frac{A_{CS} - A_S(s)}{A_{CS}} \tag{3}$$

where s is the distance from the wall, A_{CS} is the area of a control surface parallel to the wall, and $A_S(s)$ is the total area of intersection of the spheres and the control surface at a distance s from the wall. The shape and size of the control surface are chosen such that a tessellation of the shape covers the plane parallel to the wall, and each tile of the tessellation contains the same sphere geometry. The area of intersection of a single sphere with the control surface is a circle of radius, ρ, given by

$$\rho = \sqrt{\frac{d^2}{4} - \eta^2} \tag{4}$$

where η is the distance in the s direction between the sphere center and the control surface.

For the porosity in the x direction relative to the left wall in Fig. 12, let the control surface be a rectangle represented by line JK in Fig. 12, which has length $\ell = d\sqrt{3}$ in the y direction and height $h = 4d/\sqrt{6}$ in the z direction, from the center of one layers of light-colored spheres to the center of the next layer of light-colored spheres. The area of this control surface in the y–z plane is $A_{CS} = \ell h = 4d^2/\sqrt{2}$.

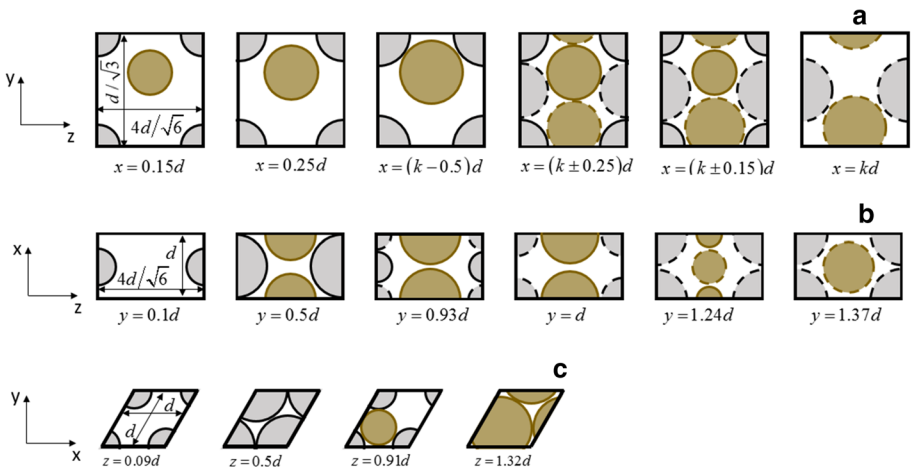

Fig. 14 Intersection of spheres with the control surfaces in **a** the y–z plane for various values of x; **b** the x–z plane for various values of y; and **c** the x–y plane for various values of z. In subplot a, the shapes with dashed outlines represent spheres centered at $x = kd$, and the shapes with solid outlines represent spheres centered at $x = (2\,k-1)\,d/2$, where $k = 1, 2, 3, \ldots$ In subplot b, the light (gray) and dark (tan) shapes with solid outlines represent spheres centered at $y = 0.5d$ and $y = 0.5d + d/(2\sqrt{3})$, respectively. The light (gray) and dark (tan) shapes with dashed outlines represent spheres centered at $y = 0.5d\left(1 + \sqrt{3}\right)$ and $y = (3 + 4\sqrt{3})d/6$, respectively. In subplot c, the spheres are centered at $z = \left(1/2 + 2j\sqrt{6}\right)d$, where j is the layer number

Figure 14a shows the control surface and the areas of intersection of spheres for various values of x. For $x<d/2$, the control surface intersects four light-colored spheres whose intersection with the control surface sum to form a complete circle and one dark-colored sphere entirely intersecting the control surface. The radius of the circles is found using (4) with $\eta=d/2-x$. For $x \geq d/2$, the control surface intersects nine spheres—six light-colored spheres and three dark-colored spheres as shown in Fig. 14a (for some x, the circles have a radius of 0 based on the value of η for that x). From trigonometry and Eqs. (3) and (4), and summation of the areas of each circle and partial circle in Fig. 14a, the areal porosity relative to the left wall is given by

$$n(x)=\begin{cases}\frac{2d^2-\pi\sqrt{2}\left(xd-x^2\right)}{2d^2} & x<d/2\\ \frac{8d^2-\pi\sqrt{2}\left(d^2+4d\,|x-kd|-8(x-kd)^2\right)}{8d^2} & (k-1/2)d\leq x<(k+1/2)d\end{cases} \tag{5}$$

for $k=1, 2, \ldots$ This porosity distribution is plotted in Fig. 3. Beyond $x=d/2$, the pattern repeats at intervals of d.

For the porosity in the y direction relative to the front wall in Fig. 12, let the control surface be a rectangle represented by line LM in Fig. 12, which has length d in the x direction and again extends in the z direction from the center of one layers of light-colored spheres to the center of the next layer of light-colored spheres. The area of this control surface in the x–z plane is $A_{CS}=4d^2/\sqrt{6}$. Figure 14b shows the control surface and the areas of intersection of the spheres for various values of y. For $y<d/\left(2\sqrt{3}\right)$ $(y<0.289d)$, the control surface partially intersects two light-colored spheres, whose areas sum to form a complete circle. For $d/\left(2\sqrt{3}\right)\leq y<d\sqrt{3}/2(0.289d\leq y<0.866d)$, the control surface partially intersects two light-colored spheres and partially intersects two dark-colored spheres, whose areas sum to form one complete light-colored circle and one complete dark-colored circle, each with a different radius. For $y\geq d\sqrt{3}/2(y\geq 0.866d)$, the control surface may partially intersect two to six light-colored spheres and may wholly or partially intersect one to three dark-colored spheres, depending on the value of y.

From trigonometry and Eqs. (3) and (4), and summation of the areas of each circle and partial circle in Fig. 14b, the areal porosity relative to the front wall is given by

$$n(y)=1-A^*_{ylw}(y)-A^*_{ydp}(y)-A^*_{ylp}(y)-A^*_{ydw}(y) \tag{6}$$

where $A^*_{yK}(y)$ is the normalized area (normalized by the control section area) for the different groups of spheres in Fig. 14b, where $K=lw$ for the whole light-colored spheres, $K=dp$ for the partial dark-colored spheres, $K=lp$ for the partial light-colored spheres, and $K=dw$ for the whole dark-colored spheres. The normalized areas are

$$\begin{aligned}
A^*_{ylw}(y)&=\frac{\pi\sqrt{6}}{4}\left[\frac{1}{4}-\left(\frac{y}{d}-\frac{1}{2}-\left(m_1-1\right)\sqrt{3}\right)^2\right] && \text{for } \left(m_1-1\right)d\sqrt{3}\leq y<d+\left(m_1-1\right)d\sqrt{3}\\
A^*_{ydp}(y)&=\frac{\pi\sqrt{6}}{4}\left[\frac{1}{4}-\left(\frac{y}{d}-\frac{1}{2}-\left(m_2-\frac{5}{6}\right)\sqrt{3}\right)^2\right] && \text{for } \left(m_2-\frac{5}{6}\right)d\sqrt{3}\leq y<d+\left(m_2-\frac{5}{6}\right)d\sqrt{3}\\
A^*_{ylp}(y)&=\frac{\pi\sqrt{6}}{4}\left[\frac{1}{4}-\left(\frac{y}{d}-\frac{1}{2}-\left(m_3-\frac{1}{2}\right)\sqrt{3}\right)^2\right] && \text{for } \left(m_3-\frac{1}{2}\right)d\sqrt{3}\leq y<d+\left(m_3-\frac{1}{2}\right)d\sqrt{3}\\
A^*_{ydw}(y)&=\frac{\pi\sqrt{6}}{4}\left[\frac{1}{4}-\left(\frac{y}{d}-\frac{1}{2}-\left(m_4-\frac{1}{3}\right)\sqrt{3}\right)^2\right] && \text{for } \left(m_4-\frac{1}{3}\right)d\sqrt{3}\leq y<d+\left(m_4-\frac{1}{3}\right)d\sqrt{3}
\end{aligned} \tag{7}$$

where $m_i = 1, 2, 3, \ldots$ This porosity distribution is plotted in Fig. 3. For $y \geq (\sqrt{3} - 1)d/\sqrt{3}$, the pattern repeats at intervals of $d\sqrt{3}/2$.

For the porosity in the z direction relative to the bottom wall, let the control surface be a trapezoid NOPQ in Fig. 12, of length d on each side. The area of $A_P = d^2\sqrt{3}/2$ in the x–y plane. Figure 14c shows the control surface and the areas of intersection of the spheres for various values of z. For all z, the control surface partially intersects four light-colored spheres whose areas sum to form a complete circle; however, depending on η, the circle may have a radius of $\rho = 0$. For $z \geq 2d/\sqrt{6} (z \geq 0.816d)$, the control surface also intersects one or three dark-colored spheres whose areas sum to form a complete circle (depending on η, the circle may have a radius of $\rho = 0$). All spheres are centered at $z = \left(1/2 + 2j\sqrt{6}\right)d$, where j is the layer number. From trigonometry and Eqs. (3) and (4), and summation of the areas of each circle and partial circle in Fig. 14c, the areal porosity relative to the bottom is given by

$$n(z) = 1 - \sum_j A^*_{zj}(z) \tag{8}$$

where $A^*_{zj}(z)$ is the normalized area (normalized by the control section area) of the spheres in Layer j as a function of z, given by

$$A^*_{zj}(z) = \frac{\pi}{2\sqrt{3}}\left[1 - \left(\frac{2z}{d} - 1 - \frac{4(j-1)}{\sqrt{6}}\right)^2\right] \quad \text{for} \quad \frac{2(j-1)}{\sqrt{6}}d \leq z < d + \frac{2(j-1)}{\sqrt{6}}d \tag{9}$$

This porosity distribution is plotted in Fig. 3. For $z \geq \left(3 - \sqrt{6}\right)d/3$, the pattern repeats at intervals of $2d/\sqrt{6}$.

As drawn in Fig. 12, the box dimensions are $N_x d \times d + \left(N_y - 1\right)d\sqrt{3}/2$ in the x–y plane, where N_x and N_y are the number of spheres in the x- and y-directions, respectively, in an odd-numbered layer. With these box dimensions, the odd-numbered layers are perfectly contained within the box. Nevertheless, the porosity is higher near the back wall than near the front wall, because the distance between the back wall and the last row of dark-colored spheres is greater than the distance between the front wall and the first row of dark-colored spheres. Thus, even for a perfectly dimensioned container, different wall effects would be observed along the two different walls in the y–z plane.

Furthermore, any rectangular prismatic box is likely not to be perfectly dimensioned, further increasing the wall effects. For example, if the box in Fig. 12 is slightly larger in the x direction, the spheres would be more loosely packed at the right wall, assuming that during packing the spheres are placed tightly along the left wall. Thus, $n(x)$ near the right wall would be higher than $n(x)$ near the left wall, leading to higher preferential flows and magnified wall effects along the right wall.

References

Carman, P.C.: Fluid flow through granular beds. Trans. Inst. Chem. Eng. **15**, 150–166 (1937)

Cohen, Y., Metzner, A.B.: Wall effects in laminar flow of fluids through packed beds. AIChE J. **27**(5), 705–715 (1981). https://doi.org/10.1002/aic.690270502

Crimaldi, J.P.: Planar laser induced fluorescence in aqueous flows. Exp. Fluids **44**(6), 851–863 (2008)

de Klerk, A.: Voidage variation in packed beds at small column to particle diameter ratio. AIChE J. **49**(8), 2022–2029 (2003). https://doi.org/10.1002/aic.690490812

Eisfeld, B., Schnitzlein, K.: The influence of confining walls on the pressure drop in packed beds. Chem. Eng. Sci. **56**(14), 4321–4329 (2001). https://doi.org/10.1016/s0009-2509(00)00533-9

Gunn, D.J.: Axial and radial dispersion in fixed-beds. Chem. Eng. Sci. **42**(2), 363–373 (1987). https://doi.org/10.1016/0009-2509(87)85066-2

Mcwhirter, J.D., Crawford, M.E., Kleins, D.E.: Wall region porosity distributions for packed beds of uniform spheres with modified and unmodified walls. Transp. Porous Media **27**, 99–118 (1997). https://doi.org/10.1023/A:1006576012179

McWhirter, J.D., Crawford, M.E., Klein, D.E.: Magnetohydrodynamic flows in porous media II: experimental results. Fusion Technol. **34**(3), 187–197 (1998)

Ogata, A., Banks, R.B.: A solution of the differential equation of longitudinal dispersion in porous media (1961)

Robbins, G.A.: Methods for determining transverse dispersion coefficients of porous media in laboratory column experiments. Water Resour. Res. **25**(6), 1249–1258 (1989). https://doi.org/10.1029/WR025i006p01249

Roth, E.J.: Experimental investigation of scalar spreading by engineered injection and extraction in porous media (2018)

Schwartz, C.E., Smith, J.M.: Flow distribution in packed beds. Ind. Eng. Chem. **45**(6), 1209–1218 (1953). https://doi.org/10.1021/ie50522a025

Smith, W.O., Foote, P.D., Busang, P.F.: Packing of homogeneous spheres. Phys. Rev. **34**(9), 1271–1274 (1929). https://doi.org/10.1103/PhysRev.34.1271

Stohr, M., Roth, K., Jahne, B.: Measurement of 3D pore-scale flow in index-matched porous media. Exp. Fluids **35**, 159–166 (2003). https://doi.org/10.1007/s00348-003-0641-x

Werth, C.J., Zhang, C., Brusseau, M.L., Oostrom, M., Baumann, T.: A review of non-invasive imaging methods and applications in contaminant hydrogeology research. J. Contam. Hydrol. **113**(1–4), 1–24 (2010). https://doi.org/10.1016/j.jconhyd.2010.01.001

Wright, S.F., Zadrazil, I., Markides, C.N.: A review of solid–fluid selection options for optical-based measurements in single-phase liquid, two-phase liquid–liquid and multiphase solid–liquid flows. Exp. Fluids **58**(9), 108 (2017). https://doi.org/10.1007/s00348-017-2386-y